

Lattice Boltzmann simulation of immiscible fluid displacement in porous media: Homogeneous versus heterogeneous pore network

Haihu Liu,^{1,2,3,a)} Yonghao Zhang,² and Albert J. Valocchi³

¹School of Energy and Power Engineering, Xi'an Jiaotong University, 28 West Xianning Road, Xi'an 710049, China

²James Weir Fluids Laboratory, Department of Mechanical and Aerospace Engineering, University of Strathclyde, Glasgow G1 1XJ, United Kingdom

³Department of Civil and Environmental Engineering, University of Illinois at Urbana-Champaign, Urbana, Illinois 61801, USA

(Received 4 August 2014; accepted 28 April 2015; published online 27 May 2015)

Injection of anthropogenic carbon dioxide (CO_2) into geological formations is a promising approach to reduce greenhouse gas emissions into the atmosphere. Predicting the amount of CO_2 that can be captured and its long-term storage stability in subsurface requires a fundamental understanding of multiphase displacement phenomena at the pore scale. In this paper, the lattice Boltzmann method is employed to simulate the immiscible displacement of a wetting fluid by a non-wetting one in two microfluidic flow cells, one with a homogeneous pore network and the other with a randomly heterogeneous pore network. We have identified three different displacement patterns, namely, stable displacement, capillary fingering, and viscous fingering, all of which are strongly dependent upon the capillary number (Ca), viscosity ratio (M), and the media heterogeneity. The non-wetting fluid saturation (S_{nw}) is found to increase nearly linearly with $\log Ca$ for each constant M . Increasing M (viscosity ratio of non-wetting fluid to wetting fluid) or decreasing the media heterogeneity can enhance the stability of the displacement process, resulting in an increase in S_{nw} . In either pore networks, the specific interfacial length is linearly proportional to S_{nw} during drainage with equal proportionality constant for all cases excluding those revealing considerable viscous fingering. Our numerical results confirm the previous experimental finding that the steady state specific interfacial length exhibits a linear dependence on S_{nw} for either favorable ($M \geq 1$) or unfavorable ($M < 1$) displacement, and the slope is slightly higher for the unfavorable displacement. © 2015 Author(s). All article content, except where otherwise noted, is licensed under a Creative Commons Attribution 3.0 Unported License. [<http://dx.doi.org/10.1063/1.4921611>]

I. INTRODUCTION

Carbon capture and storage (CCS) is a method of reducing anthropogenic emission of greenhouse gases into the atmosphere thereby mitigating global climate change. In CCS, carbon dioxide (CO_2) is captured from power plants or other large point-source emitters, purified, compressed, and injected into subsurface formations for long-term sequestration. Deep saline aquifers are considered as the most ideal candidate reservoirs for sequestering CO_2 because they are geographically widespread, have large potential capacities for storage, and are not used for water supply.¹ When CO_2 is injected into deep saline aquifers, it exists in a supercritical state and displaces the formation fluid from the pore space in a variety of possible saturation patterns, depending on the relative strength of capillary and viscous forces, as well as large and small scale geological heterogeneities.^{2–4} Fingering and displacement patterns at the pore scale strongly influence the CO_2 storage process within the

^{a)}Author to whom correspondence should be addressed. Electronic mail: haihu.liu@mail.xjtu.edu.cn

reservoir in terms of storage capacity, security, and ultimate fate of the injected CO₂. Therefore, it is of paramount importance to study and understand the mechanisms of immiscible fluid displacement in realistic porous media.

Experimental studies of immiscible fluid displacement focus on using two categories of porous media: natural media, such as rock cores and transparent network models collectively known as micromodels. Rock cores are advantageous for characterizing individual formations, but suffer from difficulty in monitoring fluids at the pore scale since sophisticated and unique micro-tomographic facilities are needed to visualize the internal distribution of the fluids within the rock cores. Moreover, it is challenging to independently manipulate porosity, pore size, connectivity, and wetting properties for natural porous media. These limitations can be overcome by micromodels, which are two-dimensional (2D) pore network patterns etched into materials such as silicon, glass, polyester resin, and most recently, polydimethylsiloxane (PDMS).⁵ Micromodels allow for visualization of fluid distribution using cameras with or without fluorescent microscopy, and subsequent quantification of fluid saturation and interfacial area may provide mechanistic insight about physical displacement process at the microscopic level. For example, Lenormand *et al.*⁶ performed a series of classic displacement experiments for several fluid pairs in an oil-wet micromodel constructed of a polymer resin, and established a phase diagram delineating parameter domains for stable displacement, capillary, and viscous fingering. They also observed “crossover” behavior in intermediate regions of their phase diagram corresponding to flow morphologies with characteristics of more than one regime. Phase diagram behavior was later demonstrated by Zhang *et al.*⁷ in a homogeneous water-wet micromodel, and their experimental results showed that the exact locations of the various region boundaries and crossover zones are dependent on the pore network. Micromodels, however, are criticized for the lack of the complex geometry of real media, which often has multi-scale and random characteristics that will dictate fluid and solute transport. Numerical simulations can complement experimental studies, providing an economic and efficient pathway to explore the influence of flow and physical parameters in various complicated porous media. However, the numerical methods based on the continuum description are insufficient to consider the influence of pore-scale parameters on the macroscopic bulk properties and, hence, the details of fingering pattern in the porous media cannot be resolved.⁸ Statistical models, i.e., Invasion Percolation (IP), Diffusion-Limited Aggregation (DLA), and anti-DLA, are able to describe certain “specialized” displacement regimes, but they cannot capture transitions from one regime to another.^{6,9}

The lattice Boltzmann method (LBM) has been developed as an attractive and promising numerical tool for pore-scale simulation of multiphase flows in porous media.^{10–14} Unlike pore-network models,^{6,15,16} which use a simplified representation of pore geometry and approximate transient flow with a steady-state Poiseuille law, LBM models complex multiphase flows in domain with realistic pore geometries. The fundamental idea of the LBM is to construct simplified kinetic models that incorporate the essential physics of microscopic or mesoscopic processes to ensure that the macroscopic averaged properties obey the desired macroscopic equations. LBM has several advantages over the conventional grid-based computational fluid dynamics (CFD) methods, such as volume-of-fluid (VOF)^{17,18} and level-set (LS) methods,^{19,20} especially in dealing with complex boundaries, incorporation of microscopic interactions, flexible reproduction of interface between multiple phases, and parallelisation of the algorithm. In the LBM community, a number of multiphase models have been proposed. These models can be classified into four types, i.e., the color-fluid model,^{21–23} the interparticle-potential model,^{24–26} the phase-field-based model,^{27,28} and the mean-field theory model.²⁹ A detailed review of these models for pore-scale flows can be found in Ref. 30.

In this paper, a recently improved color-fluid LB model²³ is used to simulate immiscible displacement of a wetting fluid by injecting a non-wetting fluid at a constant flow rate under a wide range of flow conditions in two microfluidic flow cells, one with a homogeneous pore network and the other with a randomly heterogeneous pore network. We investigate the effect of capillary number, viscosity ratio, and media heterogeneity on displacement patterns. We also quantify the fluid saturations and interfacial areas, and compare the simulation results with the experimental results of Zhang *et al.*,⁷ who conducted a series of displacement experiments in a homogeneous pore network micromodel with precisely microfabricated pore structures.

II. MODEL DESCRIPTION

The model we are using in the LB simulations is a D2Q9 two-phase lattice Bhatnagar-Gross-Krook (LBGK) algorithm, where we introduce the interfacial tension and phase segregation in accordance with the method of Liu *et al.*²³ In this model, red and blue distribution functions f_i^R and f_i^B are used to represent two different fluids. The total distribution function is defined by $f_i = f_i^R + f_i^B$, which undergoes a collision step as³¹

$$f_i^\dagger(\mathbf{x}, t) = f_i(\mathbf{x}, t) - \frac{1}{\tau} [f_i(\mathbf{x}, t) - f_i^{eq}(\mathbf{x}, t)] + \Phi_i(\mathbf{x}, t), \quad (1)$$

where $f_i(\vec{x}, t)$ is the total distribution function in the i -th velocity direction at the position \vec{x} and time t , f_i^{eq} is the equilibrium distribution function of f_i , f_i^\dagger is the post-collision distribution function, τ is the dimensionless relaxation time, and Φ_i is the perturbation term. Conservation of total mass and momentum requires

$$\rho = \sum_i f_i = \sum_i f_i^{eq}, \quad (2)$$

$$\rho \mathbf{u} = \sum_i f_i \mathbf{e}_i = \sum_i f_i^{eq} \mathbf{e}_i, \quad (3)$$

where $\rho = \rho_R + \rho_B$ is the total density with the subscripts “R” and “B” referring to the red and blue fluids, respectively, \mathbf{u} is the local fluid velocity, and \mathbf{e}_i is the lattice velocity in the i -th direction,³²

$$\mathbf{e}_i = \begin{cases} (0, 0)c, & i = 0, \\ (\cos[(i-1)\pi/2], \sin[(i-1)\pi/2])c, & i = 1-4, \\ \sqrt{2}(\cos[(2i-9)\pi/4], \sin[(2i-9)\pi/4])c, & i = 5-8. \end{cases} \quad (4)$$

The equilibrium distribution function is calculated by

$$f_i^{eq} = \rho w_i \left[1 + \frac{3}{c^2} \mathbf{e}_i \cdot \mathbf{u} + \frac{9}{2c^4} (\mathbf{e}_i \cdot \mathbf{u})^2 - \frac{3}{2c^2} \mathbf{u}^2 \right], \quad (5)$$

where w_i is the weight factor with $w_0 = 4/9$, $w_{1-4} = 1/9$, and $w_{5-8} = 1/36$. In the above equations, $c = \delta_x/\delta_t$ is the lattice speed, where δ_x is the lattice spacing and δ_t is the time step.

The perturbation term contributes to the mixed interfacial regions and creates an interfacial tension. The perturbation term reads as^{23,31}

$$\Phi_i = A |\nabla \rho^N| \left[w_i \frac{(\mathbf{e}_i \cdot \nabla \rho^N)^2}{|\nabla \rho^N|^2} - B_i \right], \quad (6)$$

where A is a parameter directly related to the interface tension, $\sigma = \frac{4}{9} A \tau c^4 \delta_t$, and ρ^N is the phase field function defined as

$$\rho^N(\mathbf{x}, t) = \frac{\rho_R(\mathbf{x}, t) - \rho_B(\mathbf{x}, t)}{\rho_R(\mathbf{x}, t) + \rho_B(\mathbf{x}, t)}, \quad -1 \leq \rho^N \leq 1. \quad (7)$$

The generalized expression for B_i is given by Liu *et al.*³¹ and it is taken as $B_0 = 2c^2/9$, $B_{1-4} = c^2/9$, and $B_{5-8} = c^2/36$ in this work.

The evaluation of $\nabla \rho^N$ is required to calculate the perturbation term, i.e., Eq. (6). To minimize the discretization error, $\nabla \rho^N$ is evaluated by Ref. 23,

$$\nabla \rho^N(\mathbf{x}, t) = \frac{3}{c^2} \sum_i w_i \rho^N(\mathbf{x} + \mathbf{e}_i \delta_t, t) \mathbf{e}_i. \quad (8)$$

Then, we use the recoloring algorithm proposed by Latva-Kokko and Rothman³³ to produce the phase segregation and guarantee the immiscibility of both fluids. Following their algorithm, the

recolored distribution functions of the red and blue fluids are

$$\begin{aligned} f_i^R(\mathbf{x}, t) &= \frac{\rho_R}{\rho} f_i^\dagger(\mathbf{x}, t) + \beta w_i \frac{\rho_R \rho_B}{\rho} \mathbf{e}_i \cdot \mathbf{n}, \\ f_i^B(\mathbf{x}, t) &= \frac{\rho_B}{\rho} f_i^\dagger(\mathbf{x}, t) - \beta w_i \frac{\rho_R \rho_B}{\rho} \mathbf{e}_i \cdot \mathbf{n}, \end{aligned} \quad (9)$$

where β is the segregation parameter and is fixed at 0.7^{34,23} and $\mathbf{n} = \nabla \rho^N / |\nabla \rho^N|$ is the unit vector normal to the interface.

After the recoloring step, the distribution functions propagate to the neighboring lattice nodes, known as propagation or streaming step,

$$f_i^k(\mathbf{x} + \mathbf{e}_i \delta_t, t + \delta_t) = f_i^k(\mathbf{x}, t), \quad k = R \text{ or } B, \quad (10)$$

with the post-propagation distribution functions being used to calculate the densities of both fluids by $\rho^k = \sum_i f_i^k$.

Through the Chapman-Enskog multiscale analysis, Eqs. (1), (9), and (10) can be reduced to the Navier-Stokes equations in the low frequency, long wavelength limit with Eqs. (5) and (6). The resulting equations are²³

$$\partial_t \rho + \nabla \cdot (\rho \mathbf{u}) = 0, \quad (11)$$

$$\partial_t(\rho \mathbf{u}) + \nabla \cdot (\rho \mathbf{u} \mathbf{u}) = -\nabla p + \nabla \cdot [\rho \nu (\nabla \mathbf{u} + \nabla \mathbf{u}^T)] + \mathbf{F}_S, \quad (12)$$

where $p = \frac{1}{3} \rho c^2$ is the pressure, $\nu = \frac{1}{3} c^2 (\tau - \frac{1}{2}) \delta_t$ is the kinematic viscosity of the fluid mixture, and \mathbf{F}_S is a volume-distributed interfacial force and is given by

$$\mathbf{F}_S = \nabla \cdot [\sigma (\mathbf{I} - \mathbf{n} \otimes \mathbf{n}) \delta_\Sigma]. \quad (13)$$

Here, $\delta_\Sigma = \frac{1}{2} |\nabla \rho^N|$ is the Dirac delta function and \mathbf{I} the second-order identity tensor.

To allow for unequal viscosities of the two fluids, we determine the viscosity of the fluid mixture by a harmonic mean

$$\frac{1}{\nu(\rho^N)} = \frac{1 + \rho^N}{2\nu_R} + \frac{1 - \rho^N}{2\nu_B}, \quad (14)$$

where ν_k ($k = R$ or B) is the kinematic viscosity of fluid k . It has been shown that Eq. (14) can ensure the continuity of viscosity flux across the interface.³¹

No-slip boundary conditions at solid walls are implemented by the halfway bounce-back scheme.³⁵ The wettability of the solid walls can be imposed by assuming that the solid wall is a mixture of two fluids, thus having a certain value of the phase field. The perturbation term in Eq. (6) becomes dependent on the properties of the neighboring solid lattice sites, resulting in a special case of the wetting boundary condition. The assigned value of the phase field at sites neighboring the wall sites can be used to modify the static contact angle of the interface.³¹ Similar approaches have been widely adopted by researchers in various multiphase LB models.^{36–40}

This two-phase LBGK model (i.e., color-fluid model) has been programmed into a computational software package in our research group and extensively validated through various test cases including verification of Laplace law, droplet deformation and breakup in simple shear flow, single bubble rising under buoyancy force, and the dynamic capillary intrusion.²³ Recently, this model was used to simulate liquid CO₂ displacement of water in a dual-permeability pore network, which reproduces three different displacement patterns observed in the previous micromodel experiments.³¹ More details concerning this two-phase LBGK model can be found in Refs. 23 and 31, which clearly indicate its capability for accurately handling immiscible fluids with variable density and viscosity ratios, as well as fluid flows in complex porous media. Therefore, the two-phase LBGK model is employed for pore-scale simulation of the drainage processes in microfluidic flow cells initially saturated with a wetting fluid, focusing mainly on the interfacial phenomena.

III. RESULTS AND DISCUSSION

According to the phase diagram proposed by Lenormand *et al.*,⁶ two-phase displacement in a micromodel, in the absence of gravitational force, can be characterized by two dimensional numbers: the capillary number (Ca) and the viscosity ratio (M). The capillary number describes the relative magnitude of viscous to capillary forces and is defined by $Ca = u_n \eta_n / \sigma \cos(\theta)$, where u_n and η_n are the mean velocity and dynamic viscosity of the advancing non-wetting fluid, respectively, and θ is the contact angle between the fluid-fluid interface and the pore wall. The viscosity ratio is defined as the ratio of the advancing non-wetting fluid viscosity to the defending wetting fluid viscosity (η_w), i.e., $M = \eta_n / \eta_w$. In addition, recent laboratory studies^{41–44} have shown the strong influence of subcore scale heterogeneities on steady-state migration patterns, spatial distributions, and fluid saturations. To gain a better understanding of pore-scale two-phase displacement mechanisms, a series of numerical simulations are conducted to study the effect of Ca and M on displacement stability and fluid saturation in a homogeneous and a heterogeneous pore networks, and the obtained results are compared to indicate the effect of media heterogeneity.

In our LB simulations, the densities of both fluids are assumed to be unity, the interfacial tension $\sigma = 0.03$ and the contact angle $\theta = 15^\circ$. Unless otherwise stated, the dynamic viscosity of the non-wetting fluid is fixed at 0.024. The inlet mean velocity and the dynamic viscosity of wetting fluid are determined by the capillary number and the viscosity ratio, respectively. To match these LB simulation parameters to their physical values, one needs to choose three reference quantities: a length scale L_0 , a time scale T_0 , and a mass scale M_0 . In this study, $L_0 = 5 \times 10^{-6}$ m, $T_0 = 3.6 \times 10^{-7}$ s, and $M_0 = 1.25 \times 10^{-13}$ kg. A simulation parameter with dimensions $[m]^{n1}[s]^{n2}[kg]^{n3}$ is multiplied by $[L_0]^{n1}[T_0]^{n2}[M_0]^{n3}$ to obtain the physical value. Following this criterion, for example, we can obtain the physical value of density ρ^{phy} by $\rho^{phy} = \rho \frac{M_0}{L_0^3} = \frac{1.25 \times 10^{-13}}{(5 \times 10^{-6})^3} = 10^3$ kg/m³, the physical value of interfacial tension σ^{phy} by $\sigma^{phy} = \sigma \frac{M_0}{T_0^2} = 0.03 \frac{1.25 \times 10^{-13}}{(3.6 \times 10^{-7})^2} = 0.0289$ N/m, and the physical value of non-wetting phase viscosity η_n^{phy} by $\eta_n^{phy} = \eta_n \frac{M_0}{L_0 T_0} = 0.024 \frac{1.25 \times 10^{-13}}{(5 \times 10^{-6}) \cdot (3.6 \times 10^{-7})} = 1.67 \times 10^{-3}$ Pa s.

A. Two-phase displacement in a homogeneous pore network

First, we investigate the invasion process of a non-wetting fluid in a two-dimensional homogeneous porous media geometry, as shown in Fig. 1(a). The porous media geometry consists of one inlet section and one outlet section, connected by a pore network, which contains a staggered periodic array of uniform circular grains, 80 μm (16 lattices) in diameter, with 97 μm pore bodies, 45 μm pore throats, and a porosity of 0.68. In order to produce fingering, small perturbations are introduced in the simulations. Specifically, the spatial location of each grain center is generated by the perfectly arranged coordinate plus a random perturbation (which obeys a uniform distribution) between -5 and 5 μm in both horizontal and vertical directions. Initially, the pore network is fully saturated with the wetting fluid. The non-wetting fluid is injected continuously at a constant flow rate at the left inlet, while a constant pressure is imposed at the right outlet. The lateral boundaries are assumed to be solid walls. After careful grid independence studies, the computational domain is chosen as 1920×1200 lu² (lu: lattice unit) with the pore network 1800 lattices in the horizontal direction. It is worth noting that the present pore network can be comparable to the one used by Zhang *et al.* in their micromodel experiments⁷ except that we have neglected the effect of depth and simulated the pore network with smaller grains and higher porosity in order to minimize the computing cost. In addition, it is expected that the choice of equal densities for both fluids has negligible influence on the results, since the displacement experiments are typically operated in a horizontally placed micromodel with small depth, where the gravity effect is largely suppressed.

A series of simulations are performed for capillary numbers ranging from $\log Ca = -5$ to $\log Ca = -3$ at two different viscosity ratios, i.e., $M = 1/12.5$ and $M = 1$. For each of the cases under consideration, the simulation is run until saturation of the non-wetting fluid reaches the

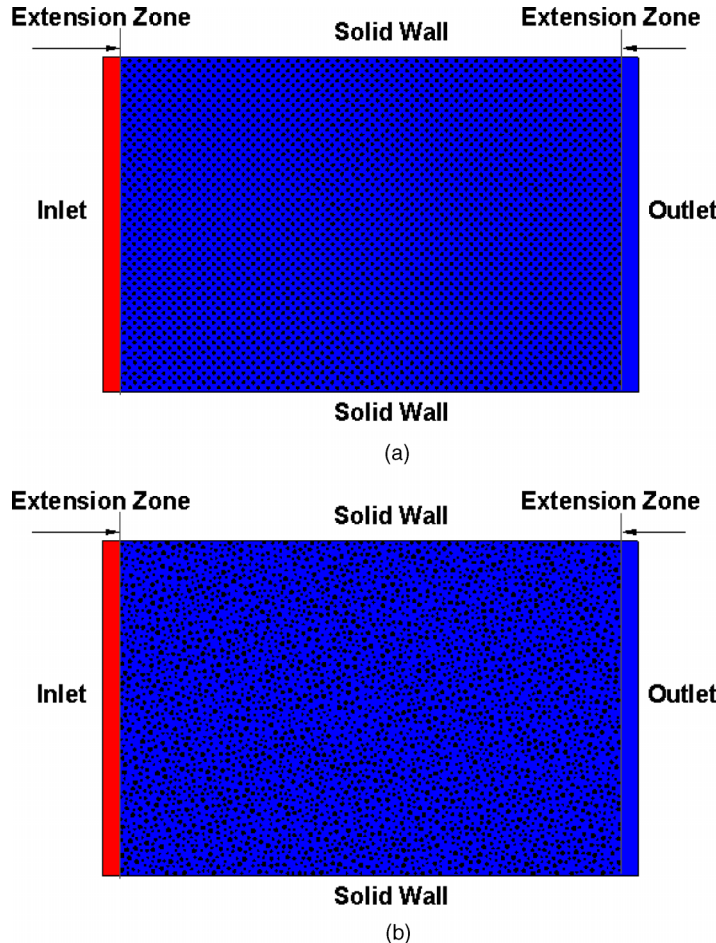


FIG. 1. Schematic diagram of (a) homogeneous and (b) heterogeneous microfluidic flow cells in the simulations and setup of the boundary conditions. The black circles represent the solid grains, while the red/lighter gray and blue/darker gray regions represent the non-wetting and wetting fluids, respectively. The size of the whole computational domain is 1920×1200 lattices for each cell.

steady state. Fig. 2 shows the final fluid distributions in the entire homogeneous flow cell at various capillary numbers for (a) $M = 1/12.5$ and (b) $M = 1$ when the non-wetting fluid is injected from the left inlet. Fingering is clearly observed during the displacement of non-wetting fluid, which is attributed to the small perturbation in position of the grains, whereas in an experiment, it may be attributed to non-uniformity in grain size, grain position, flow channel depth (3D effects), or wettability variability, all associated with the microfabrication technology. Three representative displacement patterns, namely, capillary fingering, viscous fingering, and stable displacement, are identified strongly depending on the values of capillary number and viscosity ratio. At low capillary numbers, i.e., $\log Ca = -5$, the pore body is almost occupied completely by the advancing fluid before it can reach a neighboring pore, consistent with the assumption introduced by Lenormand *et al.*⁶ in pore-network simulations. The advancing fluid flow perpendicular to the main flow direction is evident and fingers sometimes progress into new pore bodies in the backward direction, indicating capillary fingering. In capillary fingering, the invasion of non-wetting fluid is dominated by the capillary force, which causes the non-wetting fluid to progress preferentially from a pore through the largest pore throat in any direction due to a lower entry pressure. For $M = 1/12.5$ at high capillary numbers ($\log Ca > -4$), multiple loosely connected or disconnected fingers mainly progress forward toward the outlet boundary with limited or no lateral flows, and are referred to as viscous fingers. In viscous fingering, the capillary force and pressure drop over the invading fluid

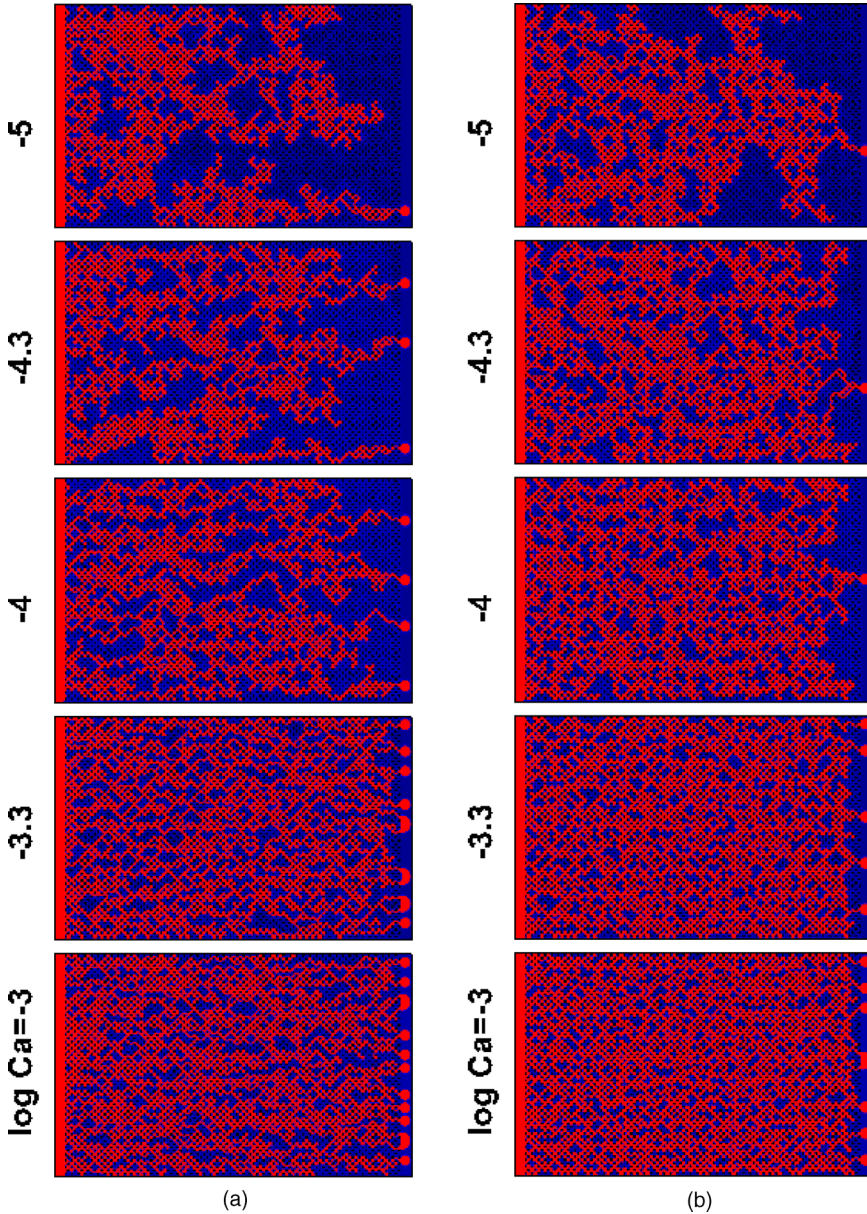


FIG. 2. Final fluid distributions in the homogeneous microfluidic flow cell at various capillary numbers for (a) $M = 1/12.5$ and (b) $M = 1$. Note that the non-wetting and wetting fluids are shown in red/lighter gray and blue/darker gray, respectively.

is negligible, and the dominant force is due to the viscosity of the wetting fluid. The dominant viscous force causes a significant fraction of fingers to occupy only partial pore bodies they pass through. At moderate capillary numbers, the unstable displacement by the less viscous non-wetting fluid shows the features of both capillary and viscous fingers. The zone where at least two types of fingers are observed is typically named as the crossover zone. For the two-phase displacement with $M = 1$, an increase in capillary number leads to the development of new flow paths that are connected to the initial finger and, hence, the interface fronts become increasingly flat, revealing some features associated with stable displacement. However, the displacement cannot fall into the regime of stable displacement even at the highest capillary number, i.e., $\log Ca = -3$, since the viscosity induced pressure drops in both invading and defending fluids are equally important. As anticipated, increasing the viscosity ratio from $M = 1/12.5$ to $M = 1$ can enhance stability during

displacement, so for $M = 1$, the fingers keep occupying completely the pore bodies that they flow through and the trapped blobs of wetting fluid are smaller in size. Finally, we can notice that the trapped blobs of wetting fluid occupy considerably more than five pore bodies at low capillary numbers; whereas, their sizes decrease with an increase in capillary number for a fixed M .

Based on the displacement patterns shown in Fig. 3, we position these simulations (represented by hollow circles) in the $\log M - \log Ca$ stability phase diagram, where we also give the boundaries of stable displacement, and capillary and viscous fingering regions established by Lenormand *et al.*⁶ (bounded by dashed lines) and by Zhang *et al.*⁷ (bounded by solid lines). As Ca increases, the immiscible displacement changes from capillary to viscous fingering for $M = 1/12.5$ ($\log M = -1.1$), but it changes from capillary fingering to near stable displacement for $M = 1$ ($\log M = 0$). This trend is consistent with the phase diagrams by Lenormand *et al.* and Zhang *et al.*, which were developed on the basis of a large number of drainage experiments for several fluid pairs in an oil-wet micromodel and in a water-wet micromodel, respectively. However, region boundaries obtained in the present pore network simulations differ from previous experimental observations. For example, our simulation with the lowest capillary number at $\log M = -1.1$ reveals considerable capillary fingering and, hence, the upper boundary of capillary fingering region should be located between $\log Ca = -5$ and $\log Ca = -4.3$, suggesting that the capillary fingering covers a region significantly different from those obtained by Lenormand *et al.*⁶ and Zhang *et al.*⁷. The differences are mainly attributed to the variations in the geometry of porous media, including porosity, pore-throat size distribution, and the size of the pore network, which will be further discussed in Sec. III B. Since we use an almost homogeneous, isotropic pore network, similar to the one used by Zhang *et al.*,⁷ it is not surprising that our obtained region boundaries are closer to Zhang *et al.*⁷ than to Lenormand *et al.*⁶

In order to quantify the displacement efficiency in the homogeneous pore network, Fig. 4 plots the steady state saturation of the non-wetting fluid (S_{nw}) as a function of $\log Ca$ for $M = 1/12.5$ and $M = 1$, which are represented by the solid and hollow circles, respectively. For each fixed M , the non-wetting fluid saturation increases with an increase in $\log Ca$, and the rate of increase is roughly a constant. The same approximately linear increase in non-wetting fluid saturation with $\log Ca$ was also reported by Cottin *et al.*⁴⁵ and Zhang *et al.*⁷ in drainage experiments, where the immiscible

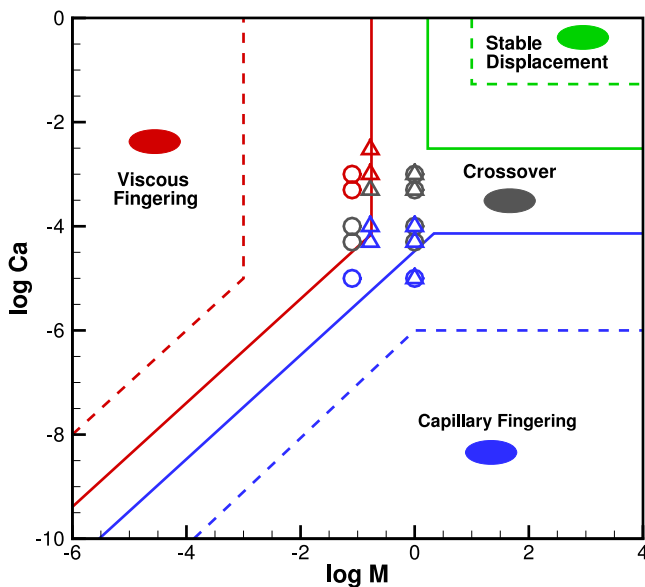


FIG. 3. $\log M - \log Ca$ phase diagram indicating the displacement patterns and the locations of the present numerical simulations (represented by discrete symbols) for immiscible displacement. Note that the hollow circles and triangles correspond to the simulations in the homogeneous and heterogeneous pore networks, respectively. The stability zones bounded by dashed and solid lines are obtained by Lenormand *et al.*⁶ and Zhang *et al.*⁷ respectively.

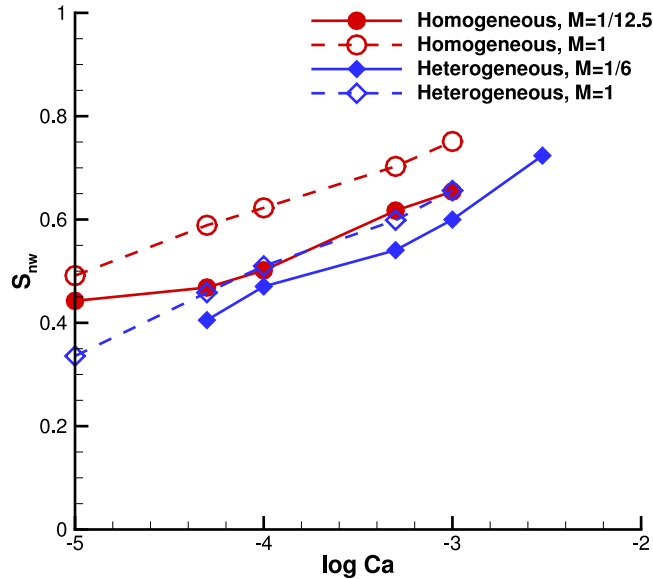


FIG. 4. Non-wetting fluid saturation as a function of the capillary number (expressed as $\log Ca$) in the homogeneous (represented by lines with circles) and heterogeneous pore networks (represented by lines with diamonds).

two-phase displacement occurs in the form of capillary and viscous fingering. In addition, it can be seen that an increase in M results in higher non-wetting fluid saturation for a fixed Ca . The increased S_{nw} is attributed to the enhanced stability of two-phase displacement, which is in accord with our numerical observations (see Fig. 2) and the phase diagram.

In addition to the fluid saturations, we also quantify the interfacial areas between the immiscible fluids. The interfacial area is an important factor influencing mass and energy transfer among phases, e.g., it can strongly influence CO_2 dissolution in the formation brine and subsequent geochemical reactions with brine and host rock in CO_2 sequestration. Following the work of Zhang *et al.*,^{7,43} we use the interfacial length instead of the interfacial area in the present 2D simulations. This length includes not only the length of interfaces between wetting and non-wetting fluids in the pore bodies and throats but also the length of the wetting films between the non-wetting fluid and the grain surfaces. Fig. 5(a) shows the variation of specific interfacial length with non-wetting fluid saturation during the displacement process, where the specific interfacial length is defined as the ratio of the interfacial length to the pore area. For each case, the specific interfacial length varies roughly linearly with S_{nw} in the entire process of displacement. All data are collapsed onto a single line except two highest Ca for $M = 1/12.5$, which exhibit a higher slope in the relationship between the specific interfacial length and S_{nw} . The higher slope is a result of viscous fingering in which some fingers are stretched very thin and even broken into small blobs, thus having a higher interfacial length than in capillary fingering and stable displacement. Similar to Refs. 7 and 43, we also plot the steady state specific interfacial length (l_s) as a function of S_{nw} , which is shown in Fig. 5(b). It is observed that l_s is linearly proportional to S_{nw} for each M , and the slope for low M ($M < 1$) is slightly higher than that for high M ($M \geq 1$), which is in good agreement with previous experimental findings of Zhang *et al.*⁷

B. Two-phase displacement in a heterogeneous random pore network

Having verified that our LB simulations can reproduce the experimental observations in a homogeneous pore network micromodel, we investigate the immiscible two-phase displacement in a heterogeneous pore network. A schematic illustration of the computational domain and boundary conditions is shown in Fig. 1(b). The heterogeneous pore network is composed of randomly distributed circular grains with the grain diameter (d) determined by

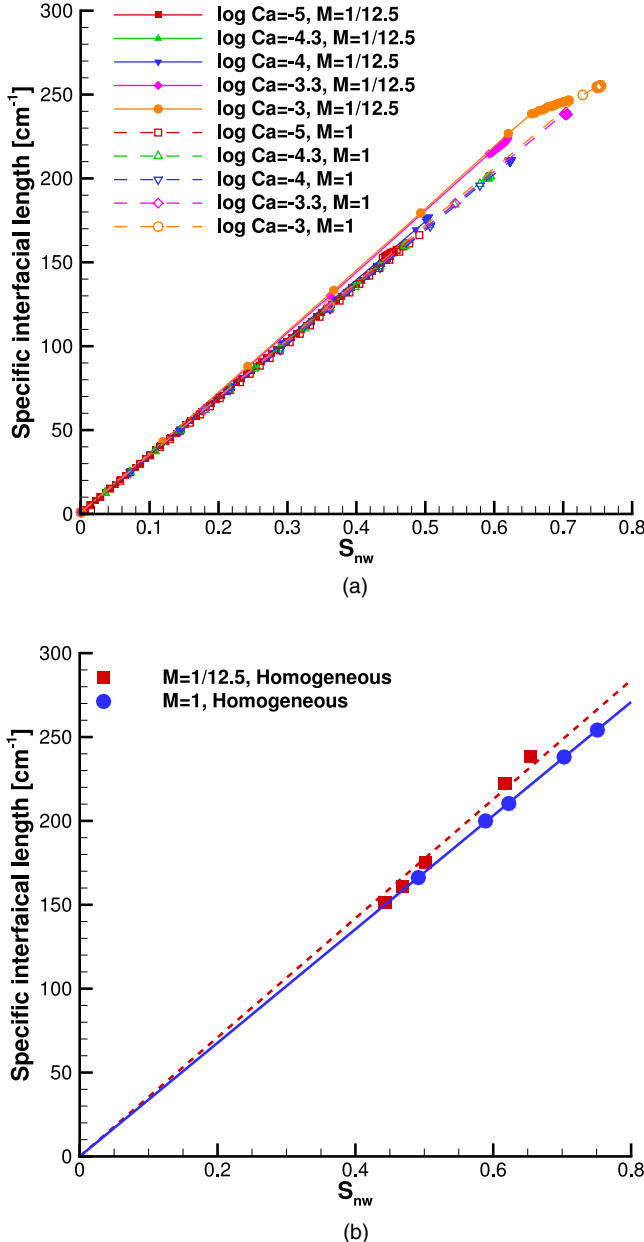


FIG. 5. Specific interfacial length (cm^{-1}) as a function of the non-wetting fluid saturation (a) during the immiscible displacement and (b) at the steady state in the homogeneous pore network. In (b), the data are fitted separately using a linear relationship for $M = 1/12.5$ and $M = 1$ with the slopes of 354.83 and 338.59, respectively.

$$d(x) = \begin{cases} d_{min}, & 0 \leq x < \delta, \\ d_{min} + \frac{d_{max} - d_{min}}{1 - 2\delta}(x - \delta), & \delta \leq x \leq 1 - \delta, \\ d_{max}, & 1 - \delta < x \leq 1, \end{cases} \quad (15)$$

where x is a uniformly distributed random number within the interval $[0, 1]$, d_{max} and d_{min} are the maximum and minimum limited values of grain diameter, and δ is a parameter between 0 and 1, which is selected to obtain the prescribed standard deviation. In our simulations, the standard deviation is $7.5 \mu\text{m}$, and d_{min} and d_{max} are taken as $60 \mu\text{m}$ and $100 \mu\text{m}$, respectively, which gives a

mean grain diameter of $80 \mu\text{m}$. To ensure sufficient computing accuracy and grid independent solutions, we assign at least 5 lattices in the gap between two neighboring grains.³¹ The pore network has the same size and porosity as the above homogeneous pore network, which allows for a direct comparison between the two-phase displacements.

Figure 6 shows the final fluid distributions in the heterogeneous microfluidic system at various Ca for $M = 1/6$ and $M = 1$. As Ca increases, for $M = 1/6$, we can clearly observe the transition from capillary to viscous fingering, which occurs at around $\log Ca = -3.3$; whereas for $M = 1$, the displacement pattern changes from capillary fingering to near stable displacement with fingers revealing some typical features associated with stable displacement when $\log Ca \geq -3.3$, such as the invaded pore bodies fully occupied by the non-wetting fluid and relatively flat advancement of the interface fronts. These observations are also reflected in $\log M - \log Ca$ phase diagram (see

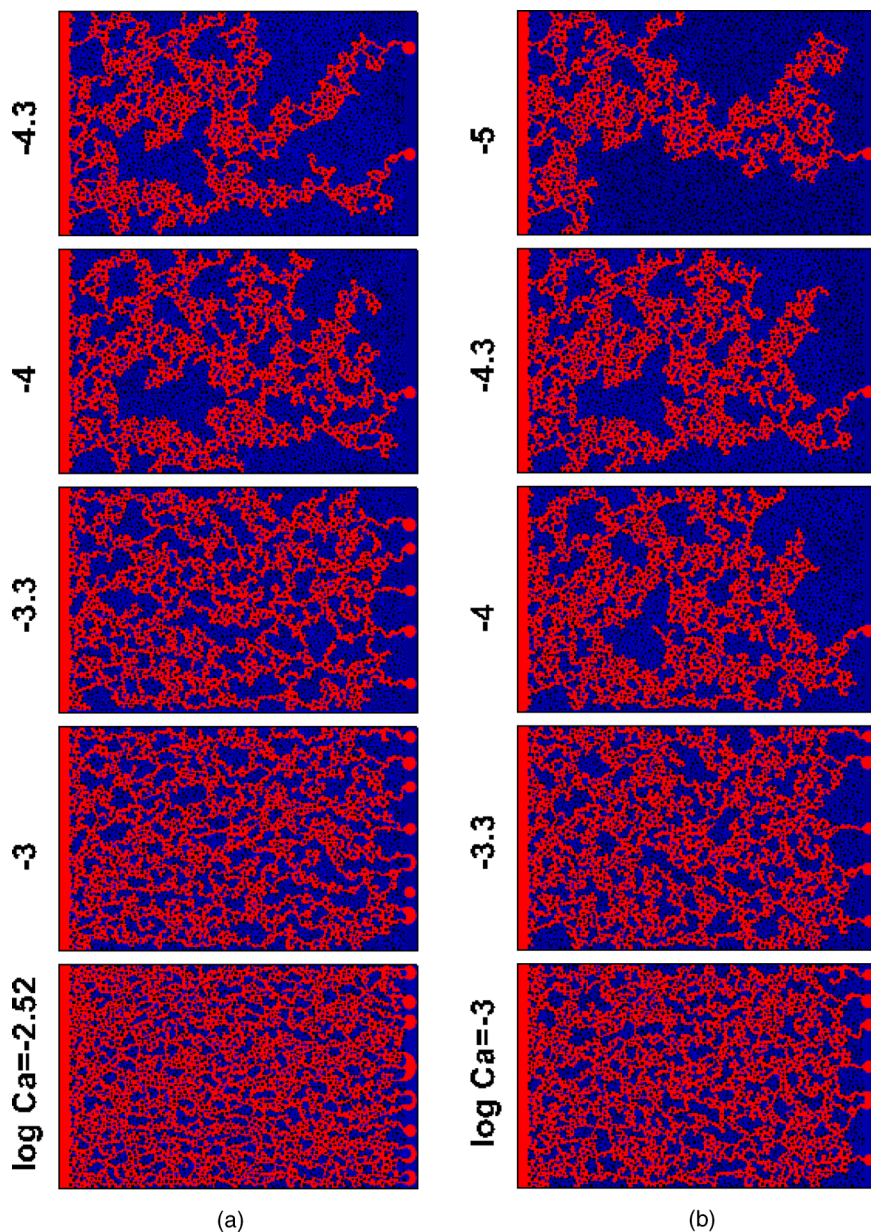


FIG. 6. Final fluid distributions in the heterogeneous microfluidic flow cell at various capillary numbers for (a) $M = 1/6$ and (b) $M = 1$. Note that the non-wetting and wetting fluids are shown in red/lighter gray and blue/darker gray, respectively.

hollow triangles in Fig. 3). In viscous fingering, i.e., $\log Ca \geq -3$ and $M = 1/6$, the dominant viscous force from the wetting fluid causes some fingers to break up, so we can see some isolated blobs of non-wetting fluid trapped in the pores. Also, these blobs decrease in size as Ca increases. In contrast, we have not seen the breakup of fingers at $\log Ca = -3$ and $M = 1/12.5$ in the homogeneous pore network (see Fig. 2) even though a lower viscosity ratio can lead to an increasingly instability. This difference is attributed to the media heterogeneity, which can promote instability of two-phase displacement. As shown in Fig. 6(b), one can observe considerable capillary fingering (evident lateral flows and back loops) for the capillary number as high as $\log Ca = -4$. Under the same flow conditions ($\log Ca = -4$ and $M = 1$) in the homogeneous pore network, however, the

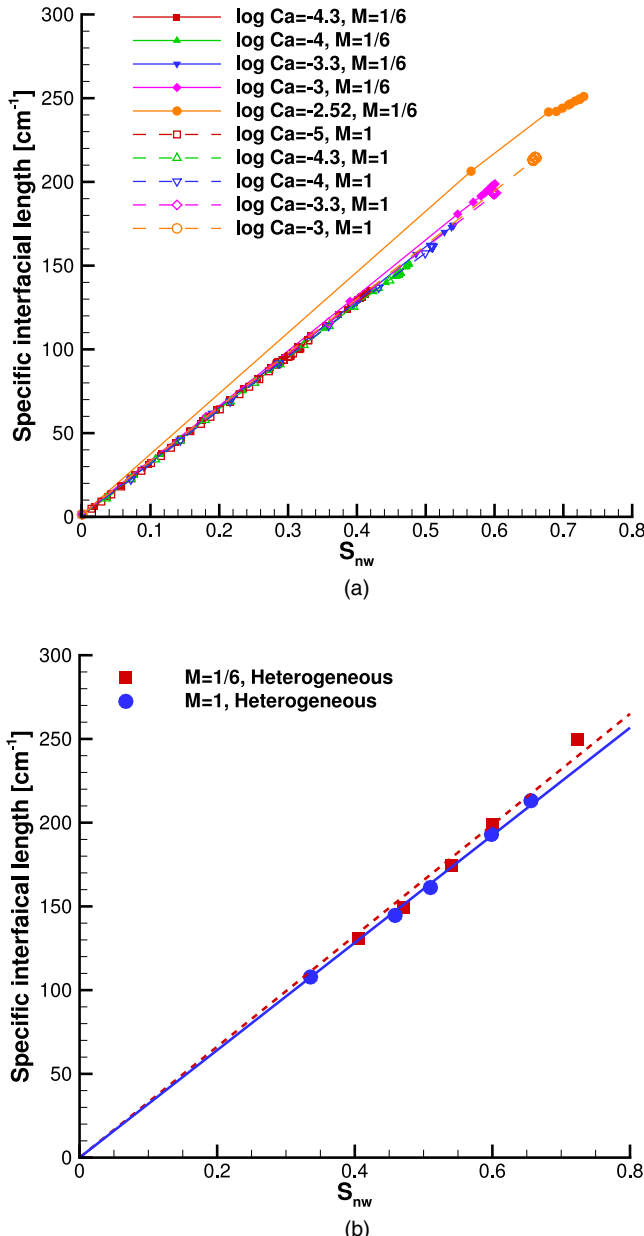


FIG. 7. Specific interfacial length (cm^{-1}) as a function of the non-wetting fluid saturation (a) during the immiscible displacement and (b) at the steady state in the heterogeneous pore network. In (b), the data are fitted separately using a linear relationship for $M = 1/6$ and $M = 1$ with the slopes of 331.25 and 320.83, respectively.

displacement is located in the crossover zone where both capillary fingering and stable displacement are observed. The different regimes also suggest that the unstable displacement is enhanced by the media heterogeneity. Finally, the residual blobs and pools of wetting fluid decrease in size with an increase in Ca for each constant M in the heterogeneous pore network, consistent with our findings in the homogeneous pore network. But it is found that the heterogeneous pore network usually leads to larger blobs and pools of wetting fluid left behind than its homogeneous counterpart.

Figure 4 also plots the steady state saturation of non-wetting fluid as a function of $\log Ca$ in the heterogeneous pore network, which is compared with the results in the previous homogeneous pore network. As observed in the homogeneous pore network, S_{nw} exhibits an approximately linear dependence on $\log Ca$ in the heterogeneous pore network for each M and also, S_{nw} is higher for a larger value of M at a fixed Ca . However, it is noticed that S_{nw} is lower in the heterogeneous pore network than in the homogeneous pore network, which results from the increased instability caused by the media heterogeneity. This can reasonably explain the conventional wisdom in reservoir engineering that heterogeneity would reduce sweep efficiency.

Fig. 7(a) presents the specific interface length as a function of S_{nw} during the invasion of a non-wetting fluid in the heterogeneous pore network for all cases investigated. Consistent with our previous observations, all data points are collapsed onto a single straight line through the origin except those indicating considerable viscous fingering, i.e., $\log Ca \geq -3$ and $M = 1/6$. It is believed that the results will deviate from the collapsed line more significantly with a further increase in Ca or a decrease in M , since both can help the growth of viscous fingering as per the $\log M - \log Ca$ phase diagram. In addition, the steady state specific interfacial length l_s exhibits a linear dependence on S_{nw} for either unfavorable ($M < 1$) or favorable ($M \geq 1$) displacement, i.e., $l_s = kS_{nw}$, where the slope k is a fitting parameter. Based on least-square fitting, the resulting equations are $l_s = 331.25S_{nw}$ and $l_s = 320.83S_{nw}$ for $M = 1/6$ and $M = 1$, respectively. Obviously, the slope for the unfavorable displacement is slightly higher than that for the favorable displacement, consistent with our numerical observation in the homogeneous pore network. From the fitting equations, it is obtained that the maximum values of l_s are 331.25 cm^{-1} and 320.8 cm^{-1} for $M = 1/6$ and $M = 1$, respectively. The maximum values of l_s are both close to the specific solid surface length 316.33 cm^{-1} (calculated as the solid surface length divided by the pore area), which occurs when

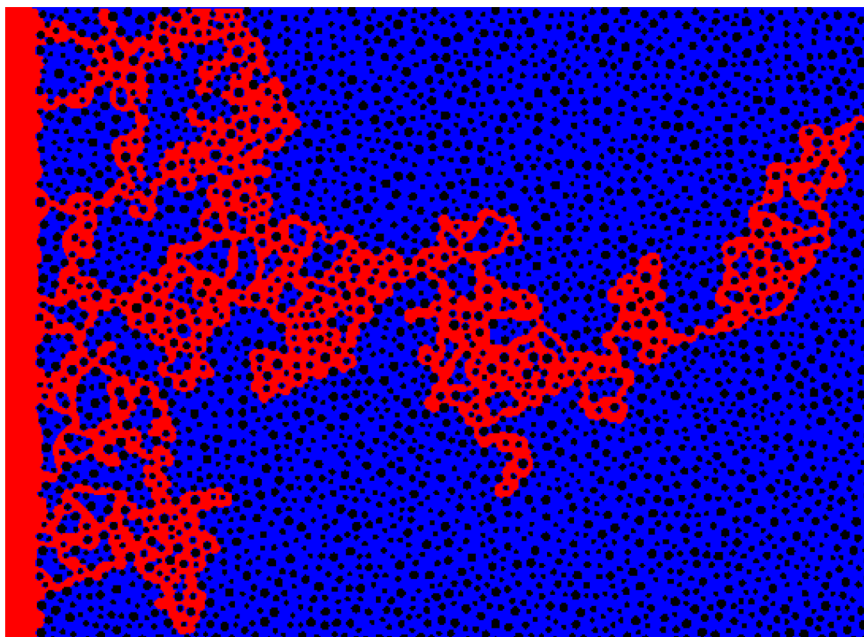


FIG. 8. Final fluid distributions in the heterogeneous microfluidic flow cell at $\log Ca = -5$ and $M = 1/25$. Note that the non-wetting and wetting fluids are shown in red/lighter gray and blue/darker gray, respectively.

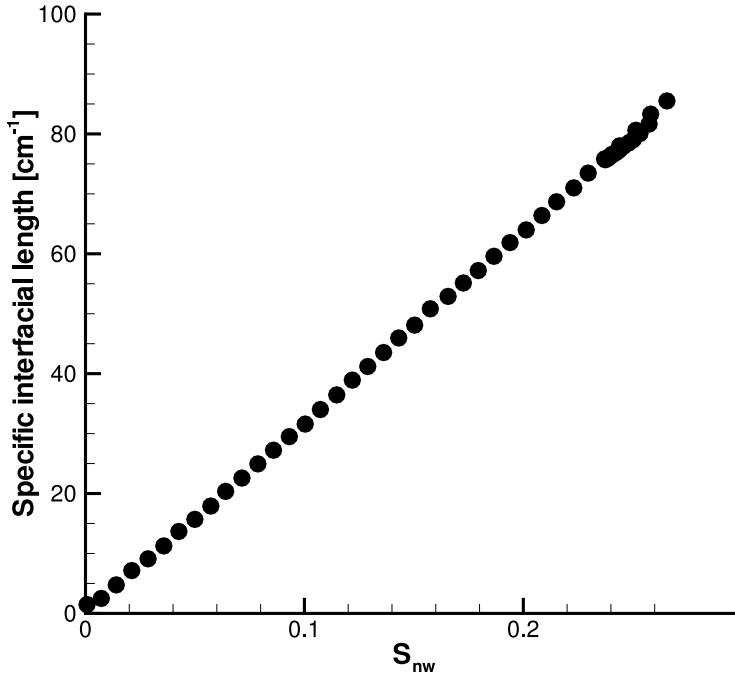


FIG. 9. Specific interfacial length (cm^{-1}) as a function of the non-wetting fluid saturation during the immiscible displacement at $\log Ca = -5$ and $M = 1/25$.

the non-wetting fluid occupies all of the pore space, i.e., $S_{nw} = 1$. The linear relationship between specific interfacial area and non-wetting fluid saturation has also been shown experimentally in one-dimensional column studies during drainage.^{46–48}

As we know, it is still challenging to simulate a wide range of viscosity ratios for many existing multiphase LB models.³⁰ To examine the range of viscosity ratios that the present model can access, we simulate the displacement of a more viscous fluid by a less viscous one in the heterogeneous pore network at $\log Ca = -5$. The dynamic viscosities of both fluids are chosen as $\eta_n = \{0.005, 0.01, 0.02, 0.04\}$ and $\eta_w = \{0.1, 0.3, 0.5\}$ in which η_w is limited to not more than 0.5 because as η (or τ) increases, so does the Knudsen number (defined as the ratio of the mean free path to the characteristic length scale). It is found that regardless the value of η_w , the model remains stable for $\nu_n \geq 0.02$, but becomes unstable for $\nu_n < 0.02$. Thus, the lowest viscosity ratio that the present two-phase LBGK model can access is $M = \frac{0.02}{0.5} = 1/25$. Fig. 8 shows the final fluid distributions in the heterogeneous microfluidic system at $\log Ca = -5$ and $M = 1/25$. It is clearly seen that the two-phase displacement exhibits evident capillary fingering. As expected, the steady state saturation of non-wetting fluid $S_{nw} = 0.235$ is much lower than that for $\log Ca = -5$ and $M = 1$. In addition, the specific interfacial length l_s is linearly dependent on S_{nw} during the displacement (see Fig. 9), consistent with the previous observation in Fig. 7(a). To simulate lower viscosity ratios, one of feasible approaches is to replace the present LBGK model with a multiple-relaxation-time (MRT) model.⁴⁹ It has been recently demonstrated that the color-fluid MRT model can simulate the immiscible two-phase displacement with the viscosity ratios ranging from 1/200 to 500.⁵⁰

IV. CONCLUSIONS

In this work, our recently developed color-fluid LB model²³ is used for pore-scale simulation of the drainage process in two microfluidic flow cells, one with a homogeneous pore network and the other with a randomly heterogeneous pore network, which have the same size, porosity, and mean grain diameter. The extent and behavior of preferential flow (i.e., fingering) is found to depend on the capillary number (Ca), viscosity ratio (M) and media heterogeneity, and three different

displacement patterns observed in the previous micromodel experiments are reproduced: for $M \geq 1$ at low Ca , displacement occurs in the form of capillary fingering due to the dominant capillary force, and the displacement gradually becomes stable with increasing Ca ; for $M < 1$ at low Ca , capillary fingering is again exhibited, but viscous fingering dominates at higher Ca because of the lower viscosity of the displacing non-wetting fluid. In the $\log M - \log Ca$ stability phase diagram, our simulation results show that the boundaries of displacement regimes (i.e., predominantly stable displacement, and capillary and viscous fingering) are different for the homogeneous and heterogeneous pore networks, and their boundaries of regimes also differ from those obtained by Zhang *et al.*⁷ and Lenormand *et al.*⁶ due to difference in the configuration of the micromodel pore network. This suggests that the location of each regime boundary needs to be estimated by performing experimental or numerical studies on each specific pore network. For a fixed M , the non-wetting fluid saturation (S_{nw}) increases roughly linearly with $\log Ca$, consistent with the experimental observations by Cottin *et al.*⁴⁵ and Zhang *et al.*⁷ S_{nw} is higher for a larger value of M since an increase in M can enhance the stability of the displacement process. On the contrary, media heterogeneity weakens the displacement stability, resulting in lower S_{nw} in the heterogeneous pore network than in the homogeneous one. During the invasion process of the non-wetting fluid in either pore networks, the specific interfacial length is linearly proportional to S_{nw} with an identical proportionality constant for all cases except those primarily showing viscous fingering. This is because some viscous fingers can only occupy partial pore bodies that they pass through and even break up to form small blobs, leading to a larger interfacial length. As observed in the micromodel experiments of Zhang *et al.*,⁷ the steady state specific interfacial length and S_{nw} can be well correlated by a linear relationship for either favorable ($M \geq 1$) or unfavorable ($M < 1$) displacement, and the slope for the unfavorable displacement is slightly higher than that for the favorable displacement.

A recent pore-scale experimental study⁵¹ quantified the strong velocity variations in single- and multiphase flows within a three-dimensional porous media. Although the pore space is highly disordered and complex, it was found that the velocity magnitudes and the velocity components both along and transverse to the imposed flow direction are exponentially distributed. In future, we will develop a three-dimensional high-performance computing code to examine whether our LB simulations can reasonably capture the experimental findings.

ACKNOWLEDGMENTS

The authors gratefully acknowledge the support of the International Institute for Carbon Neutral Energy Research (WPI-I2CNER), sponsored by the Japanese Ministry of Education, Culture, Sports, Science and Technology. This work is also financially supported by the Engineering and Physical Sciences Research Council (EPSRC) of the UK under Grant Nos. EP/I036117/1 and EP/I011927/1. Y.H.Z. would also like to thank the UK's Royal Academy of Engineering (RAE) and the Leverhulme Trust for the award of a RAE/Leverhulme Senior Research Fellowship.

¹ IPCC, *IPCC Special Report on Carbon Dioxide Capture and Storage* (Cambridge University Press, New York, 2005).

² O. Oloruntobi and T. LaForce, "Effect of aquifer heterogeneity on CO₂ sequestration," in *Proceedings of the SPE EUROPEC/EAGE Annual Conference and Exhibition* (Society of Petroleum Engineers, Amsterdam, The Netherlands, 2009), p. SPE 121776.

³ M. Riazi, M. Sohrabi, C. Bernstone, M. Jamilahmady, and S. Ireland, "Visualisation of mechanisms involved in CO₂ injection and storage in hydrocarbon reservoirs and water-bearing aquifers," *Chem. Eng. Res. Des.* **89**(9), 1827–1840 (2011).

⁴ S. Iglauer, *Dissolution Trapping of Carbon Dioxide in Reservoir Formation Brine—A Carbon Storage Mechanism* (InTech, 2011), Chap. 10, pp. 233–262.

⁵ J. W. Grate, M. G. Warner, J. W. Pittman, K. J. Dehoff, T. W. Wietsma, C. Zhang, and M. Oostrom, "Silane modification of glass and silica surfaces to obtain equally oil-wet surfaces in glass-covered silicon micromodel applications," *Water Resour. Res.* **49**(8), 4724–4729, doi:10.1002/wrcr.20367 (2013).

⁶ R. Lenormand, E. Touboul, and C. Zarcone, "Numerical models and experiments on immiscible displacements in porous media," *J. Fluid Mech.* **189**, 165–187 (1988).

⁷ C. Zhang, M. Oostrom, T. Wietsma, J. Grate, and M. Warner, "Influence of viscous and capillary forces on immiscible fluid displacement: Pore-scale experimental study in a water-wet micromodel demonstrating viscous and capillary fingering," *Energy Fuels* **25**(8), 3493–3505 (2011).

⁸ Y. Cinar, A. Riaz, and H. Tchelepi, "Experimental study of CO₂ injection into saline formations," *SPE J.* **14**, 588–594 (2009).

- ⁹ U. Bandaraa, A. Tartakovsky, M. Oostrom, B. Palmer, J. Grate, and C. Zhang, "Smoothed particle hydrodynamics pore-scale simulations of unstable immiscible flow in porous media," *Adv. Water Resour.* **62**, 356–369 (2013).
- ¹⁰ C. Pan, M. Hilpert, and C. Miller, "Lattice-Boltzmann simulation of two-phase flow in porous media," *Water Resour. Res.* **40**, W01501, doi:10.1029/2003wr002120 (2004).
- ¹¹ M. C. Sukop and D. Or, "Lattice Boltzmann method for modeling liquid–vapor interface configurations in porous media," *Water Resour. Res.* **40**, W01509, doi:10.1029/2003WR002333 (2004).
- ¹² J. F. Chau and D. Or, "Linking drainage front morphology with gaseous diffusion in unsaturated porous media: A lattice Boltzmann study," *Phys. Rev. E* **74**, 056304 (2006).
- ¹³ H. Huang and X.-Y. Lu, "Relative permeabilities and coupling effects in steady-state gas-liquid flow in porous media: A lattice Boltzmann study," *Phys. Fluids* **21**, 092104 (2009).
- ¹⁴ H. Liu, A. J. Valocchi, Q. Kang, and C. Werth, "Pore-scale simulations of gas displacing liquid in a homogeneous pore network using the lattice Boltzmann method," *Transp. Porous Media* **99**, 555–580 (2013).
- ¹⁵ M. Blunt and P. King, "Relative permeabilities from two- and three-dimensional pore-scale network modelling," *Transp. Porous Media* **6**(4), 407–433 (1991).
- ¹⁶ M. Piri and M. J. Blunt, "Three-dimensional mixed-wet random pore-scale network modeling of two- and three-phase flow in porous media. I. Model description," *Phys. Rev. E* **71**, 026301 (2005).
- ¹⁷ A. Q. Raeini, M. J. Blunt, and B. Bijeljic, "Modelling two-phase flow in porous media at the pore scale using the volume-of-fluid method," *J. Comput. Phys.* **231**, 5653–5668 (2012).
- ¹⁸ A. Ferrari and I. Lunati, "Direct numerical simulations of interface dynamics to link capillary pressure and total surface energy," *Adv. Water Resour.* **57**, 19–31 (2013).
- ¹⁹ M. Prodanović and S. Bryant, "A level set method for determining critical curvatures for drainage and imbibition," *J. Colloid Interface Sci.* **304**(2), 442–458 (2006).
- ²⁰ E. Jettestuen, J. O. Helland, and M. Prodanović, "A level set method for simulating capillary-controlled displacements at the pore scale with nonzero contact angles," *Water Resour. Res.* **49**(8), 4645–4661, doi:10.1002/wrcr.20334 (2013).
- ²¹ A. K. Gunstensen, D. H. Rothman, S. Zaleski, and G. Zanetti, "Lattice Boltzmann model of immiscible fluids," *Phys. Rev. A* **43**(8), 4320–4327 (1991).
- ²² T. Reis and T. N. Phillips, "Lattice Boltzmann model for simulating immiscible two-phase flows," *J. Phys. A: Math. Theor.* **40**(14), 4033–4053 (2007).
- ²³ H. Liu, A. J. Valocchi, and Q. Kang, "Three-dimensional lattice Boltzmann model for immiscible two-phase flow simulations," *Phys. Rev. E* **85**, 046309 (2012).
- ²⁴ X. Shan and H. Chen, "Lattice Boltzmann model for simulating flows with multiple phases and components," *Phys. Rev. E* **47**(3), 1815–1819 (1993).
- ²⁵ X. Shan and H. Chen, "Simulation of nonideal gases and liquid-gas phase transitions by the lattice Boltzmann equation," *Phys. Rev. E* **49**, 2941 (1994).
- ²⁶ M. Sbragaglia, R. Benzi, L. Biferale, S. Succi, K. Sugiyama, and F. Toschi, "Generalized lattice Boltzmann method with multirange pseudopotential," *Phys. Rev. E* **75**, 026702 (2007).
- ²⁷ M. R. Swift, W. R. Osborn, and J. M. Yeomans, "Lattice Boltzmann simulation of nonideal fluids," *Phys. Rev. Lett.* **75**(5), 830–833 (1995).
- ²⁸ M. R. Swift, E. Orlandini, W. R. Osborn, and J. M. Yeomans, "Lattice Boltzmann simulations of liquid-gas and binary fluid systems," *Phys. Rev. E* **54**(5), 5041–5052 (1996).
- ²⁹ X. He, S. Chen, and R. Zhang, "A lattice Boltzmann scheme for incompressible multiphase flow and its application in simulation of Rayleigh–Taylor instability," *J. Comput. Phys.* **152**(2), 642–663 (1999).
- ³⁰ H. Liu, Q. Kang, C. R. Leonardi, B. D. Jones, S. Schmieschek, A. Narváez, J. R. Williams, A. J. Valocchi, and J. Harting, "Multiphase lattice Boltzmann simulations for porous media applications—A review," *Comput. Geosci.* (to be published); e-print [arXiv:1404.7523](https://arxiv.org/abs/1404.7523).
- ³¹ H. Liu, A. J. Valocchi, C. Werth, Q. Kang, and M. Oostrom, "Pore-scale simulation of liquid CO₂ displacement of water using a two-phase lattice Boltzmann model," *Adv. Water Resour.* **73**, 144–158 (2014).
- ³² Y. H. Qian, D. D’Humières, and P. Lallemand, "Lattice BGK models for Navier–Stokes equation," *Europhys. Lett.* **17**, 479–484 (1992).
- ³³ M. Latva-Kokko and D. H. Rothman, "Diffusion properties of gradient-based lattice Boltzmann models of immiscible fluids," *Phys. Rev. E* **71**, 056702 (2005).
- ³⁴ I. Halliday, A. P. Hollis, and C. M. Care, "Lattice Boltzmann algorithm for continuum multicomponent flow," *Phys. Rev. E* **76**, 026708 (2007).
- ³⁵ A. J. C. Ladd, "Numerical simulations of particulate suspensions via a discretized Boltzmann equation. (Part I & II)," *J. Fluid Mech.* **271**, 285–339 (1994).
- ³⁶ S. Bekri and P. M. Adler, "Dispersion in multiphase flow through porous media," *Int. J. Multiphase Flow* **28**(4), 665–697 (2002).
- ³⁷ S. van der Graaf, T. Nisisako, C. G. P. H. Schroën, R. G. M. van der Smagt, and R. M. Boom, "Lattice Boltzmann simulations of droplet formation in a T-shaped microchannel," *Langmuir* **22**, 4144–4152 (2006).
- ³⁸ N. S. Martys and H. Chen, "Simulation of multicomponent fluids in complex three-dimensional geometries by the lattice Boltzmann method," *Phys. Rev. E* **53**, 743–750 (1996).
- ³⁹ A. G. Yiotis, J. Psihogios, M. E. Kainourgiakis, A. Papaioannou, and A. K. Stubos, "A lattice Boltzmann study of viscous coupling effects in immiscible two-phase flow in porous media," *Colloids Surf., A* **300**, 35–49 (2007).
- ⁴⁰ H. Liu and Y. Zhang, "Droplet formation in microfluidic cross-junctions," *Phys. Fluids* **23**, 082101 (2011).
- ⁴¹ J.-C. Perrin and S. Benson, "An experimental study on the influence of sub-core scale heterogeneities on CO₂ distribution in reservoir rocks," *Transp. Porous Media* **82**, 93–109 (2010).
- ⁴² J.-Q. Shi, Z. Xue, and S. Durucan, "Supercritical CO₂ core flooding and imbibition in tako sandstone—Influence of sub-core scale heterogeneity," *Int. J. Greenhouse Gas Control* **5**(1), 75–87 (2011).

- ⁴³ C. Zhang, M. Oostrom, J. W. Grate, T. W. Wietsma, and M. G. Warner, "Liquid CO₂ displacement of water in a dual-permeability pore network micromodel," *Environ. Sci. Technol.* **45**(17), 7581–7588 (2011).
- ⁴⁴ M. Wu, F. Xiao, R. M. Johnson-Paben, S. T. Retterer, X. Yin, and K. B. Neeves, "Single- and two-phase flow in microfluidic porous media analogs based on Voronoi tessellation," *Lab Chip* **12**, 253–261 (2012).
- ⁴⁵ C. Cottin, H. Bodiguel, and A. Colin, "Drainage in two-dimensional porous media: From capillary fingering to viscous flow," *Phys. Rev. E* **82**, 046315 (2010).
- ⁴⁶ M. L. Brusseau, S. Peng, G. Schnaar, and M. S. Costanza-Robinson, "Relationships among air–water interfacial area, capillary pressure, and water saturation for a sandy porous medium," *Water Resour. Res.* **42**(3), W03501, doi:10.1029/2005wr004058 (2006).
- ⁴⁷ A. F. Anwar, M. Bettahar, and U. Matsubayashi, "A method for determining air–water interfacial area in variably saturated porous media," *J. Contam. Hydrol.* **43**(2), 129–146, (2000).
- ⁴⁸ M. L. Porter, D. Wildenschild, G. Grant, and J. I. Gerhard, "Measurement and prediction of the relationship between capillary pressure, saturation, and interfacial area in a NAPL-water-glass bead system," *Water Resour. Res.* **46**(8), W08512, doi:10.1029/2009WR007786 (2010).
- ⁴⁹ P. Lallemand and L.-S. Luo, "Theory of the lattice Boltzmann method: Dispersion, dissipation, isotropy, galilean invariance, and stability," *Phys. Rev. E* **61**(6), 6546–6562 (2000).
- ⁵⁰ H. Huang, J.-J. Huang, and X.-Y. Lu, "Study of immiscible displacements in porous media using a color-gradient-based multiphase lattice Boltzmann method," *Comput. Fluids* **93**, 164–172 (2014).
- ⁵¹ S. S. Datta, H. Chiang, T. S. Ramakrishnan, and D. A. Weitz, "Spatial fluctuations of fluid velocities in flow through a three-dimensional porous medium," *Phys. Rev. Lett.* **111**, 064501 (2013).